Disorder-induced phase transitions in double HgTe quantum wells

Sergey Krishtopenko, A. Ikonnikov, Benoit Jouault, Frederic Teppe

Disorder-induced phase transitions in double HgTe quantum wells

S. S. Krishtopenko,[1,*] A. V. Ikonnikov,[2,*] B. Jouault,[1] and F. Teppe[1,†]

[1] *Laboratoire Charles Coulomb (L2C), UMR 5221 CNRS-Université de Montpellier, F-34095 Montpellier, France*
[2] *Physics Department, M.V. Lomonosov Moscow State University, Moscow, 119991, Russia*

(Dated: August 28, 2023)

By using the self-consistent Born approximation, we investigate disorder effect induced by short-range impurities on the band-gap of a seminal two-dimensional (2D) system, whose phase diagram contains trivial, single-band-inverted and double-band-inverted states. Following the density-of-states (DOS) evolution, we demonstrate multiple closings and openings of the band-gap with the increase of the disorder strength. Calculations of the spectral function describing the quasiparticles at the Γ point of the Brillouin zone evidence that the observed band-gap behavior is unambiguously caused by the topological phase transitions due to the mutual inversions between the first and second electron-like and hole-like subbands. We also find that an increase in the disorder strength in the double-inverted state always leads to the band-gap closing due to the overlap of the tails of DOS from conduction and valence subbands.

I. INTRODUCTION

The band structure of HgTe quantum wells (QWs) in the vicinity of the Γ point of the Brillouin zone is represented by the Dirac fermions with additional terms quadratic in quasimomentum[1]. The inherent property of these fermions is that their band-gap can be varied from positive to negative values and vice versa by changing the QW width[2–4], temperature[5–8] or hydrostatic pressure[9]. The negative band-gap values in HgTe QWs correspond to the so-called *inverted* band structure, at which the lowest electron-like level $E1$ lies below the top hole-like level $H1$, resulting in quantum spin Hall insulator (QSHI)[10,11]. This topologically non-trivial state is characterized by a bulk band-gap and a pair of helical gapless states at the edges that leads to quantized values of the conductance. Such conductance quantization is the key evidence to experimentally confirm the non-trivial topology of 2D system[11–13].

Unexpectedly, Li *et al.*[14] discovered by numerical simulations that initially clean HgTe QWs with trivial band ordering can also feature a quantized conductance value in the presence of disorder. This disordered state with quantized conductance was called as *topological Anderson insulator* (TAI). Later, Groth *et al.*[15] have explained the TAI mechanism as disorder-induced band inversion arising due to the presence of quadratic terms in the Dirac-like low-energy Hamiltonian of HgTe QWs[1]. In this sense, the phenomenology of TAI is very similar to that of the QSHI. Interestly, the discovered transition correspond to weak-disorder topological transition, and thus can be treated within the self-consistent Born approximation (SCBA)[15–18]. By now, disorder-induced phase transitions have also been studied in 3D topological insulators[19–21], various topological semimetals[22–26], and even in amorphous solids[27].

A distinctive feature of all these works[19–27] is that the theoretical investigations were performed within the framework of the so-called two-band approximation, which allows describing the disorder-induced evolution of only the conduction and valence band edges. In this case, questions naturally arise: (i) how the disorder affect the edges of the higher-lying conduction and valence bands beyond the two-band models; and (ii) whether the disorder may cause a double-band inversion between second electron- and hole-like bands. These double-band-inverted states are now of interest in the context of higher-order topology[29–31].

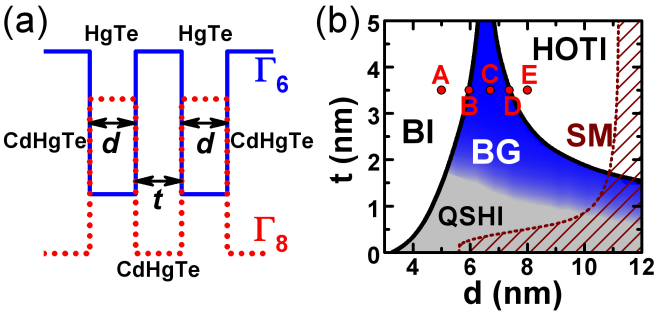

FIG. 1. (a) Schematic representation of *symmetric* double HgTe QW. Here, d is the thickness of HgTe layers and t is the middle CdHgTe barrier thickness. The double QW is assumed to be grown on (001) CdTe buffer with 30% of Hg content in all the barriers[28]. (b) The phase diagrams for different d and t obtained by numerical calculations based on eight-band $\mathbf{k}\cdot\mathbf{p}$ Hamiltonian[9]. The left-hand and right-hand solid curves correspond to the crossing between $E1$–$H1$ subbands and $E2$–$H2$ subbands, respectively. These curves divide the plane into three parts with trivial band ordering (left-hand white region), single band inversion (grey and blue regions) and double-band inversion (right-hand white region). The striped region defines a semimetal (SM) phase with vanishing *indirect* band-gap. The red symbols mark the double QWs considered in this work.

In this work, considering double HgTe QWs as a seminal example, we study disorder-induced phase transitions in a 2D system, whose phase diagram contains trivial, single-band-inverted and double-band-inverted states[28] (see Fig. 1). Different types of these states were previously probed in realistic samples by magnetotransport[32–38] and mid-infrared Landau level spec-

troscopy[39–42]. By using the SCBA and four-band 2D low-energy Hamiltonian, describing topological phase transition in double HgTe QWs[28,43], we directly calculate the DOS and spectral function visualizing quasiparticle picture at the Γ point of the Brillouin zone. By following the DOS evolution with increasing of the disorder strength, we unambiguously demonstrate multiple topological phase transitions caused by the mutual inversion of both the first and second electron-like and hole-like subbands. As a source of the disorder, we consider the electrostatic potential of randomly distributed short-range impurities, which makes it possible to reduce the system of self-consistent integral equations to an algebraic one.

II. PHASE DIAGRAM

Let us first overview the phase diagram of double HgTe QWs in the absence of disorder. In what follows, we consider a symmetrical QW grown on (001) CdTe buffer consisting of two d thick HgTe layers separated by a t thick $Cd_{0.7}Hg_{0.3}Te$ barrier (see Fig. 1). The phase diagram of double HgTe QWs was obtained on the basis of of eight-band $\mathbf{k}\cdot\mathbf{p}$ Hamiltonian[9] for the envelope wave functions, which takes into account the interaction between Γ_6, Γ_8, and Γ_7 bands in bulk materials. The calculation details and material parameters can be found in Ref.[28].

Unlike single HgTe QWs[1], the low-energy physics of double HgTe QWs is determined by the mutual arrangement of four levels at once – two electron-like ($E1$, $E2$) and two hole-like ($H1$, $H2$) subbands. Depending on the thickness of the HgTe layers and the width of the tunneling barrier, different subband arrangements at the Γ point of the Brillouin zone can be implemented. In the diagram of double HgTe QWs, the left-hand black solid curve representing the crossing between the first electron-like $E1$ and hole-like $H1$ subbands divides the d-t plane into a white region, corresponding to band insulator (BI) with trivial band ordering, and a grey region of QSHI with inverted band structure. If the middle barrier is thick enough, in addition to QSHI, the double HgTe QW also hold a specific state with a band structure similar to the one of bilayer graphene (BG) represented by the blue region in Fig. 1(b). The BG state with the $E2$-$H1$-$H2$-$E2$ level sequence (see Fig. 2(c)) was previously discussed in details in Ref.[28].

A further increase of d results in the band crossing between the second electron-like ($E2$) and hole-like ($H2$) subbands, which is represented by the right-hand black solid curve in the diagram. This curve, in its turn, separates the grey and blue regions with single band inversion from the right-hand white region corresponding to the double band inversion, when two electron-like $E1$ and $E2$ levels lie below two hole-like $H1$ and $H2$ subbands (the $H1$-$H2$-$E2$-$E1$ sequence). Recently, such double-inversion insulator state has been identified as a higher-order topological insulator (HOTI)[43] with the corner states directly attributed to the cubic symmetry of zinc-blende semiconductors. Finally, at certain d and t values corresponding to the striped region, the so-called semimetal (SM) phase is implemented. The SM state is characterized by a vanishing *indirect* band-gap when the side maxima of the valence subband exceed in energy the conduction subband bottom[44]. Thus, by varying the layer thicknesses in double HgTe QWs, one can indeed realize BI, QSHI, BG state, HOTI or SM state. Typical band dispersions of double HgTe QWs arising at different thicknesses of the HgTe layer are shown in Fig. 2.

The multiple band inversions in double HgTe QWs at the Γ point of the Brillouin zone can be explicitly described by means of effective four-band 2D low-energy Hamiltonian[28]. Within the following sequence of the basis states $|E1+\rangle$, $|H1+\rangle$, $|H2-\rangle$, $|E2-\rangle$, $|E1-\rangle$, $|H1-\rangle$, $|H2+\rangle$, $|E2+\rangle$, the effective 2D Hamiltonian for the states in the vicinity of the Γ point has the form[43]:

$$H_{2D}(\mathbf{k}) = \begin{pmatrix} H_{4\times4}(k_x,k_y) & 0 \\ 0 & H^*_{4\times4}(-k_x,-k_y) \end{pmatrix}, \quad (1)$$

where $\mathbf{k}=(k_x,k_y)$ is quasimomentum in the QW plane and the asterisk denotes complex conjugation. The diagonal blocks of $H_{2D}(\mathbf{k})$, in turn, are split into isotropic and anisotropic parts:

$$H_{4\times4}(\mathbf{k}) = H^{(i)}_{4\times4}(\mathbf{k}) + H^{(a)}_{4\times4}(\mathbf{k}). \quad (2)$$

The isotropic term $H^{(i)}_{4\times4}(\mathbf{k})$ preserves the rotational symmetry in the QW plane, therefore it is independent of the orientation of x and y axis. On the contrary, the anisotropic term $H^{(a)}_{4\times4}(\mathbf{k})$ results from the cubic symmetry of zinc-blende semiconductors, and depends not only on the QW growth orientation but also on the orientation of x and y axes. Since we are not interested in describing higher-order topological bound states arising due to the crystal symmetry of zinc-blende semiconductors[43], we will further neglect $H^{(a)}_{4\times4}(\mathbf{k})$. Its explicit form for (001)-oriented QWs can be found elsewhere[43]. Additionally, we also neglect the terms resulting from the anisotropy of chemical bonds at the QW interfaces[44] and the bulk inversion asymmetry of the unit cell of zinc-blende semiconductors[45]. These terms do not play significant role in HgTe-based heterostructures[3,46–50], while in their absence, $H_{2D}(\mathbf{k})$ takes the block-diagonal form.

The isotropic part of $H_{4\times4}(\mathbf{k})$ in Eq. (2) is written as[28]:

$$H^{(i)}_{4\times4}(\mathbf{k}) = \begin{pmatrix} \epsilon_{E1} & -A_1k_+ & R^{(i)}_1k^2_- & S_0k_- \\ -A_1k_- & \epsilon_{H1} & 0 & R^{(i)}_2k^2_- \\ R^{(i)}_1k^2_+ & 0 & \epsilon_{H2} & A_2k_+ \\ S_0k_+ & R^{(i)}_2k^2_+ & A_2k_- & \epsilon_{E2} \end{pmatrix}, \quad (3)$$

where

$$\begin{aligned} \epsilon_{E1}(k_x,k_y) &= C_1 + M_1 - (D_1+B_1)(k_x^2+k_y^2), \\ \epsilon_{H1}(k_x,k_y) &= C_1 - M_1 - (D_1-B_1)(k_x^2+k_y^2), \\ \epsilon_{E2}(k_x,k_y) &= C_2 + M_2 - (D_2+B_2)(k_x^2+k_y^2), \\ \epsilon_{H2}(k_x,k_y) &= C_2 - M_2 - (D_2-B_2)(k_x^2+k_y^2). \end{aligned} \quad (4)$$

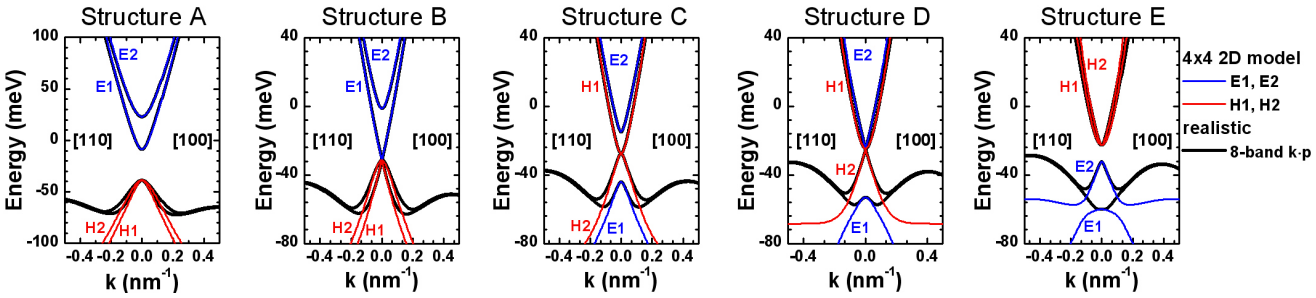

FIG. 2. Band structure of double HgTe QWs with $t = 3.5$ nm. The values of d are marked by red symbols in Fig. 1. The bold black curves correspond to realistic band structure calculations on the basis of eight-band $\mathbf{k}\cdot\mathbf{p}$ Hamiltonian[9]. The thin curves represent the energy-dispersion for electron-like (in blue) and hole-like (in red) subbands calculated by using the *isotropic part* of $H_{4\times4}(\mathbf{k})$. The positive and negative values of $\mathbf{k}$ correspond to the [100] and [110] crystallographic orientations, respectively. The parameters for $H_{4\times4}(\mathbf{k})$ are provided in Table I.

TABLE I. Structure parameters involved in *isotropic part* of $H_{4\times4}(\mathbf{k})$ in Eq. (2) for double HgTe/CdHgTe QWs, whose layer thicknesses are represented by red symbols in Fig. 1. We also note that $C_2 = C_1 - M_1 + M_2$. The structure parameter for an arbitrary thickness of the HgTe layers in the range from 5.0 nm to 8.00 nm can be obtained by interpolation between the values presented in the table.

Structure	d (nm)	t (nm)	C_1 (meV)	M_1 (meV)	M_2 (meV)	B_1 (meV·nm^2)	B_2 (meV·nm^2)	D_1 (meV·nm^2)
A	5.00	3.50	-23.73	15.04	30.91	-494.80	-397.54	-422.00
B	5.97	3.50	-31.37	0.00	15.00	-669.41	-537.84	-600.85
C	6.70	3.50	-35.73	-8.32	6.25	-851.05	-615.76	-786.85
D	7.37	3.50	-38.88	-14.20	0.00	-1071.75	-694.25	-1012.46
E	8.00	3.50	-41.34	-18.74	-4.82	-1431.86	-777.63	-1378.16

Structure	D_2 (meV·nm^2)	A_1 (meV·nm)	A_2 (meV·nm)	$R_1^{(i)}$ (meV·nm^2)	$R_2^{(i)}$ (meV·nm^2)	S_0 (meV·nm)
A	-321.67	405.08	391.19	67.50	-92.96	-2.94
B	-465.37	387.65	372.25	90.64	-108.30	0.05
C	-546.76	374.07	358.11	116.53	-121.70	2.43
D	-629.15	361.40	-345.31	-405.09	-135.09	4.73
E	-716.99	348.99	-333.11	-501.63	-148.81	7.04

Here, $k_\pm = k_x \pm ik_y$, k_x and k_y are the momentum components in the QW plane, and $C_{1,2}$, $M_{1,2}$, $A_{1,2}$, $B_{1,2}$, $D_{1,2}$, S_0 and $R_{1,2}^{(i)}$ are *isotropic* structure parameters being defined by the QW geometry, the growth orientation and the layer materials. As can be seen from their physical meaning, the parameters S_0 and $R_{1,2}^{(i)}$, which describe the coupling between the HgTe layers, vanish if $t \to \infty$.

The most important quantities in $H_{2D}(k_x, k_y)$ are two mass parameters M_1 and M_2 describing the band inversion between $E1$–$H1$ subbands and $E2$–$H2$ subbands, respectively. The trivial BI corresponds to positive values of M_1 and M_2. The QSHI and BG states arise if $M_1 < 0$ and $M_2 > 0$, and the difference between these states is defined by the gap between the $H1$ and $H2$ subbands[28]. The HOTI state with double band inversion is represented by negative values of M_1 and M_2. We note that since the SM phase represented by the striped areas in the diagram of Fig. 1 is formed by an overlap at non-zero quasimomentum of the valence and conduction subbands, it cannot be described within the low-energy Hamiltonian valid for the states at the small values of k_x and k_y.

Figure 2 also compares the band structure calculations based on the realistic eight-band $\mathbf{k}\cdot\mathbf{p}$ Hamiltonian[9] and $H_{2D}(\mathbf{k})$ in Eq. (1) for double HgTe QWs with $t = 3.5$ nm at several values of d (marked by the red symbols in the phase diagram of Fig. 1). One can see a good agreement between the results from both models at small values. One can see good agreement between the results of both models for small quasimomentum values. The structural parameters used in the calculations are summarized in Tab. I.

III. SCBA FOR DOUBLE HGTE QWS

So far, we have discussed the "clean" case of double HgTe QWs. In this section, we focus on the theoretical description of the disorder effect on the band ordering of double HgTe QWs, caused by randomly distributed impurities in the QW plane. Since we are interested in the topological phase transitions induced by weak disorder,

we will treat them within the self-consistent Born approximation[15–18]. Further, we represent the calculations for the upper block of $H_{2D}(\mathbf{k})$ in Eq. (1), while the calculations for the lower block are performed in the same way.

Let us consider Green's function defined by

$$\hat{G}(\mathbf{k},\varepsilon) = \langle \frac{1}{\varepsilon - \mathcal{H}} \rangle = \Big[\varepsilon - H_{4\times4}(\mathbf{k}) - \hat{\Sigma}(\mathbf{k},\varepsilon)\Big]^{-1}, \quad (5)$$

with

$$\mathcal{H} = H_{4\times4}(\mathbf{k}) + V_{imp}(\mathbf{r}), \quad (6)$$

where $\langle ... \rangle$ denotes average over all disorder configurations, and $\hat{\Sigma}(\mathbf{k},\varepsilon)$ is the self-energy matrix. In Eq. (6), we have also introduced a disorder potential $V_{imp}(\mathbf{r})$, consisting of randomly distributed individual impurities:

$$V_{imp}(\mathbf{r}) = \sum_j v(\mathbf{r} - \mathbf{R}_j),\ v(\mathbf{r}) = \int \frac{d^2\mathbf{q}}{(2\pi)^2} \tilde{v}(\mathbf{q}) e^{i\mathbf{q}\cdot\mathbf{r}}, \quad (7)$$

where R_j denotes position of impurities and $v(\mathbf{r})$ is the potential of an individual impurity, which is assumed to be isotropic, i.e., $\tilde{v}(\mathbf{q}) = \tilde{v}(q)$ with $|\mathbf{q}| = q$.

In the absence of $H^{(a)}_{4\times4}(\mathbf{k})$, which is neglected in Eq. (2), $H_{4\times4}(\mathbf{k})$ possesses full rotational symmetry, and its wave-function can be presented in the form:

$$\Psi_{4\times4}(\mathbf{k}) = U(\theta_\mathbf{k})^{-1} \Psi_{4\times4}(k), \quad (8)$$

where $k = |\mathbf{k}|$, $k_x = k\cos\theta_\mathbf{k}$, $k_y = k\sin\theta_\mathbf{k}$,

$$U(\theta) = \begin{pmatrix} 1 & 0 & 0 & 0 \\ 0 & e^{i\theta} & 0 & 0 \\ 0 & 0 & e^{-2i\theta} & 0 \\ 0 & 0 & 0 & e^{-i\theta} \end{pmatrix}. \quad (9)$$

Therefore, the Green's function in Eq. (5) can be presented in the form

$$\hat{G}(\mathbf{k},\varepsilon) = U(\theta_\mathbf{k}) \hat{G}(k,\varepsilon) U(\theta_\mathbf{k})^{-1}, \quad (10)$$

with

$$\hat{G}(k,\varepsilon) = \Big[\varepsilon - \tilde{H}_{4\times4}(k) - \hat{\Sigma}(k,\varepsilon)\Big]^{-1}, \quad (11)$$

which depends only on k. This shows that $\hat{G}(\mathbf{k},\varepsilon)$ depends on the angle via the terms of $U(\theta_\mathbf{k})$. We note that $\tilde{H}_{4\times4}(k)$ differs from $H_{4\times4}(\mathbf{k})$ by

$$\tilde{H}_{4\times4}(k) = U(\theta_\mathbf{k}) H_{4\times4}(\mathbf{k}) U(\theta_\mathbf{k})^{-1}. \quad (12)$$

Within the SCBA, the self-energy matrix in Eq. (5) has a form

$$\hat{\Sigma}(\mathbf{k},\varepsilon) = n_i \int \frac{d^2\mathbf{k}'}{(2\pi)^2} \tilde{v}(\mathbf{k}-\mathbf{k}') \hat{G}(\mathbf{k}',\varepsilon) \tilde{v}(\mathbf{k}'-\mathbf{k}), \quad (13)$$

where n_i is the concentration of impurities. Similar to Eq. (8), the self-energy matrix can be represented as

$$\hat{\Sigma}(\mathbf{k},\varepsilon) = U(\theta_\mathbf{k}) \hat{\Sigma}(k,\varepsilon) U(\theta_\mathbf{k})^{-1}, \quad (14)$$

with a matrix $\hat{\Sigma}(k,\varepsilon)$ written as

$$\hat{\Sigma}(k,\varepsilon) = n_i \int_0^{K_c} \frac{k'dk'}{2\pi} \times \begin{pmatrix} V_0^2 G'_{11} & V_{-1}^2 G'_{12} & V_{+2}^2 G'_{13} & V_{+1}^2 G'_{14} \\ V_{+1}^2 G'_{21} & V_0^2 G'_{22} & V_{+3}^2 G'_{23} & V_{+2}^2 G'_{24} \\ V_{-2}^2 G'_{31} & V_{-3}^2 G'_{32} & V_0^2 G'_{33} & V_{-1}^2 G'_{34} \\ V_{-1}^2 G'_{41} & V_{-2}^2 G'_{42} & V_{+1}^2 G'_{43} & V_0^2 G'_{44} \end{pmatrix}. \quad (15)$$

Here, $G'_{ij} \equiv G_{ij}(k',\varepsilon)$ are the component of the averaged Green's function in Eq. (11), and $V_n^2 \equiv V_n(k,k')^2$ are defined as

$$V_n(k,k')^2 = \int_0^{2\pi} \frac{d\theta}{2\pi} |\tilde{v}(\mathbf{k}-\mathbf{k}')|^2 \cos n\theta. \quad (16)$$

Importantly, in Eq. (15), we introduce a cut-off wavevector $K_c = \pi/a_0$ (where a_0 is the lattice constant in the QW plane, which is actually the lattice constant of the CdTe buffer), corresponding to the edge of 2D Brillouin zone (cf. Ref.[26]). This naturally limits the integration over quasimomentum k.

Once the Green's function is known, one can calculate the spectral function $A(k,\varepsilon)$ and density-of-states $D(\varepsilon)$:

$$A(k,\varepsilon) = -\frac{1}{\pi} \mathrm{Im} \left\{ \mathrm{Tr} \left(\hat{G}(k,\varepsilon + i0) \right) \right\},$$
$$D(\varepsilon) = g_S \int_0^{K_c} \frac{kdk}{2\pi} A(k,\varepsilon), \quad (17)$$

where the factor $g_S = 2$ takes into account the contribution from the lower block in Eq. (1). The density-of-states $D(\varepsilon)$ provides the most direct way to trace the evolution of the effective band-gap as a function of the impurity scattering, while $A(k,\varepsilon)$ represents the renormalization of the quasiparticle spectral properties at a given disorder strength.

As clear, Eqs. (11) and (15) form a system of integral equations that defines the Green's function matrix $\hat{G}(k,\varepsilon)$. The self-consistent solution of such integral systems in the general case is a laborious task. However, for some particular cases of randomly distributed individual impurities, the solution of the problem can be greatly simplified. To proceed further, we assume $\tilde{v}(q) = u_0$, which corresponds to the disorder formed by the short-range impurities:

$$v(\mathbf{r}) = \int_0^\infty \frac{qdq}{2\pi} \tilde{v}(q) \int_0^{2\pi} \frac{d\theta}{2\pi} e^{iqr\cos\theta} = \frac{u_0}{2\pi} \frac{\delta(r)}{r}. \quad (18)$$

In this case, $V_n(k,k')^2 = u_0^2 \delta_{n,0}$ in Eq. (16), resulting in a diagonal form of the self-energy matrix in Eq. (15):

$$\hat{\Sigma}(\varepsilon) = \begin{pmatrix} \Sigma_{E1}(\varepsilon) & 0 & 0 & 0 \\ 0 & \Sigma_{H1}(\varepsilon) & 0 & 0 \\ 0 & 0 & \Sigma_{H2}(\varepsilon) & 0 \\ 0 & 0 & 0 & \Sigma_{E2}(\varepsilon) \end{pmatrix} = \frac{W^2}{4\pi} \int_0^{K_c^2} dx \begin{pmatrix} G_{11}(\sqrt{x},\varepsilon) & 0 & 0 & 0 \\ 0 & G_{22}(\sqrt{x},\varepsilon) & 0 & 0 \\ 0 & 0 & G_{33}(\sqrt{x},\varepsilon) & 0 \\ 0 & 0 & 0 & G_{44}(\sqrt{x},\varepsilon) \end{pmatrix}, \tag{19}$$

where we define the disorder strength as $W^2 = n_i u_0^2$. The self-energy independence from k allows for an analytical calculation of the integrals in Eq. (19).

Indeed, first of all, we note that the determinant of the matrix $\left[\varepsilon - \tilde{H}_{4\times4}(\sqrt{x}) - \hat{\Sigma}(\varepsilon)\right]$ for the case of short-range impurities is represented as a polynomial of the fourth degree in x:

$$\left|\varepsilon - \tilde{H}_{4\times4}(\sqrt{x}) - \hat{\Sigma}(\varepsilon)\right| = A_4(\varepsilon)x^4 + A_3(\varepsilon)x^3 + A_2(\varepsilon)x^2 + A_1(\varepsilon)x + A_0(\varepsilon), \tag{20}$$

where $A_4(\varepsilon)$, $A_3(\varepsilon)$, $A_2(\varepsilon)$, $A_1(\varepsilon)$ and $A_0(\varepsilon)$ are complex functions, found by straightforward calculation of 4×4 symmetric matrix determinant.

Second, the diagonal components of the Green's function $G_{ii}(\sqrt{x},\varepsilon)$ $(i = 1...4)$ in Eq. (19) are presented as

$$G_{ii}\left(\sqrt{x},\varepsilon\right) = \frac{a_i(\varepsilon)x^3 + b_i(\varepsilon)x^2 + c_i(\varepsilon)x + d_i(\varepsilon)}{\left|\varepsilon - \tilde{H}_{4\times4}(\sqrt{x}) - \hat{\Sigma}(\varepsilon)\right|}, \tag{21}$$

where the terms a_i, ... d_i are independent of x. This last equation can be verified by the direct calculation of the inverse matrix $\left[\varepsilon - \tilde{H}_{4\times4}(\sqrt{x}) - \hat{\Sigma}(\varepsilon)\right]^{-1}$. As the self-energy matrix has imaginary part, all the coefficients in Eq. (21) are complex as well.

In order to calculate the integrals in Eq. (19), we have numerically found the roots x_1, x_2, x_3, x_4 of the polynomial needed for the following expansion:

$$A_4x^4 + A_3x^3 + A_2x^2 + A_1x + A_0 = A_4(x - x_1)(x - x_2)(x - x_3)(x - x_4) \tag{22}$$

with A_0, ... A_4 are independent of x. Although the values of x_1, x_2, x_3, x_4 can be found analytically by means of *Ferrari's method*, the numerical procedures also allow for the calculations with any needed degree of accuracy. Once the roots are known, the integrals are calculated analytically (see Appendix). In this case, this self-consistent system of integral equations is transformed into the set of algebraic equations, which can be numerically solved by iteration procedure.

Finally, the spectral function $A(k,\varepsilon)$ and density-of-states $D(\varepsilon)$ for the case of the short-range disorder can be written as

$$A(k,\varepsilon) = -\frac{1}{\pi}\mathrm{Im}\left\{\sum_{i=1}^{4} G_{ii}(k,\varepsilon)\right\},$$
$$D(\varepsilon) = -\frac{g_S}{W^2\pi}\mathrm{Im}\left\{\mathrm{Tr}\left(\hat{\Sigma}(\varepsilon)\right)\right\}. \tag{23}$$

We remind that in order to take into account the contribution from the lower block in Eq. (1), one should set the degeneracy factor of DOS as $g_S = 2$.

IV. RESULTS AND DISCUSSION

As known for "conventional" HgTe/CdHgTe QWs[1–4], if the QW has a trivial band ordering in the "clean" limit, the presence of disorder leads to the band inversion and disorder-induced topological phase transition[14,15]. A similar behavior can also be expected for double HgTe QWs with a thick opaque barrier. In the latter case, the 2D system is described by two identical copies of Bernevig-Hughes-Zhang (BHZ) model[1] (see Eq. (3)), each of which corresponding to one of the HgTe QWs with parameters S_0 and $R_{1,2}^{(i)}$ set to zero for the inter-layer coupling. In the presence of a tunnel-transparent barrier, that actually leads to a rich phase diagram in Fig. 1, the BHZ-like blocks "1" and "2" of $H_{4\times4}(\mathbf{k})$ in Eq. (3) cease to be identical and become coupled due to non-zero parameters S_0 and $R_{1,2}^{(i)}$. Nevertheless, even in this case, it is reasonable to expect a disorder-induced inversion both between subband pairs of $E1$ and $H1$, and between $E2$ and $H2$.

Figure 3(a) shows the evolution of DOS with the disorder strength $W = \sqrt{n_i}u_0$ for double HgTe QW with BI state in the "clean" limit (the structure "A" in Fig. 2 and Tab. I with positive mass parameters M_1 and M_2). As clear, the band-gap in the DOS decreases with W until it vanishes above a critical value W_{c1}, and then it is reopened again at $W > W_{c2}$ (see black regions in Fig. 3(a) where the DOS vanishes). In the range $W_{c1} \leq W \leq W_{c2}$, the double QW remains gapless, which is well illustrated by the non-zero DOS in Fig. 3(b). With a further increase in disorder strength, the newly opened gap closes again at $W \simeq 350$ meV·nm. Further, we demonstrate that such behavior of the DOS is directly attributed to the disorder effect on the electronic states at the Γ point of the Brillouin zone.

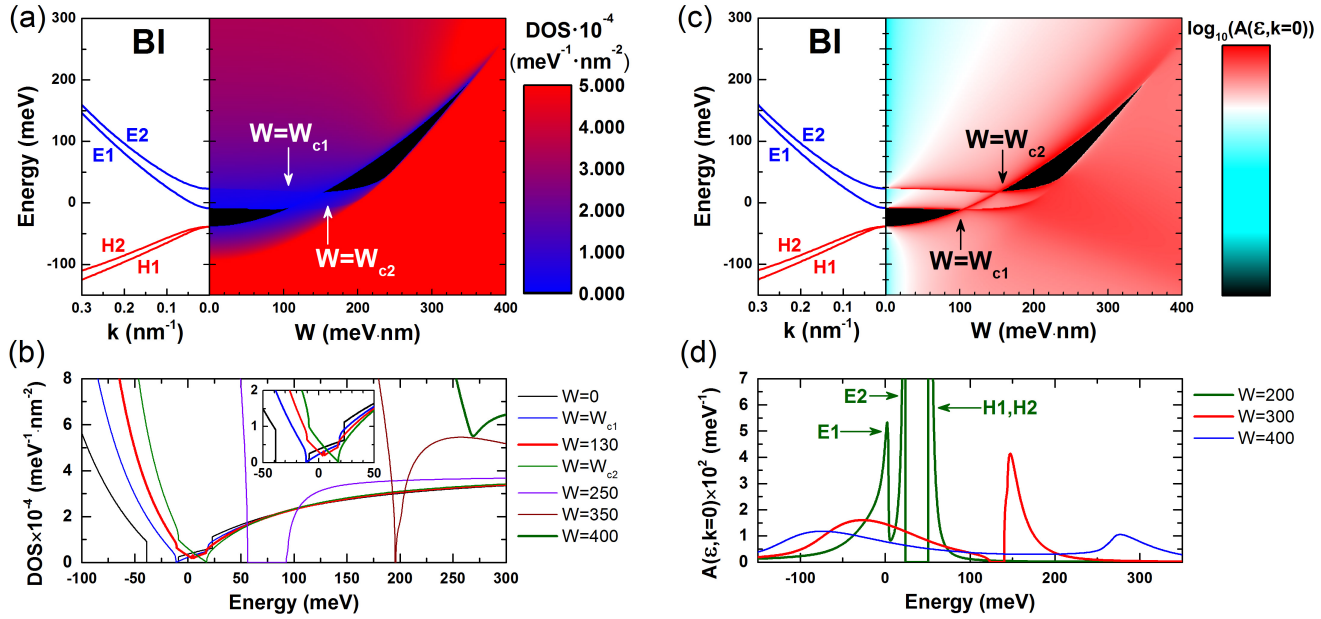

FIG. 3. (a) Band structure and color map of the DOS as a function of the disorder strength $W = \sqrt{n_i}u_0$ calculated for double HgTe QW which has a BI state in the "clean" limit (see the structure "A" in Fig. 1). (b) The DOS as a function of energy at different values of W. The inset shows in more detail the DOS behavior at $W_{c1} \leq W \leq W_{c2}$. (c) Band structure and color map of the spectral function at the Γ point $A(k = 0, \varepsilon)$ for the same double HgTe QW. (d) Energy dependence of $A(k = 0, \varepsilon)$ at different disorder strength $W > W_{c2}$.

In order to shed light on this point, let us now consider a spectral function $A(k, \varepsilon)$ describing quasiparticle properties at given disorder strength. As clear, at $W = 0$ corresponding to the "clean" 2D system, the spectral function is represented by sum of δ-functions centered at the the eigenvalue energies of $H_{4\times4}(\mathbf{k})$ in Eq. (2). Although the spectral function $A(k, \varepsilon)$ widens in the presence of disorder, its maximum values are still representative of the quasiparticle energy dispersion, while its broadening in the vicinity of the maxima values define the quasiparticle lifetime[26].

Figure 3(c) provides a disorder-induced evolution of the spectral function at the Γ point, which perfectly reproduces two band-gap regions arising in the DOS. As can be seen from the color map unambiguously identifying the subband edges, the first band-gap closing at $W = W_{c1}$ is indeed attributed to the mutual inversion of $E1$ and $H1$ subbands. As clear, the band-gap opening at $W = W_{c2}$ is also related to the band inversion but in the second pair of $E2$ and $H2$ subbands. Thus, the points with $W = W_{c1}$ and $W = W_{c2}$ indeed represent topological transitions into a gapless state with single band inversion and into an double-inverted insulator, respectively. The latter can be naturally attributed to the analog of the HOTI state in the clean limit[43]. Moreover, since the edges of $H1$ and $H2$ subbands still coincide on the color map, a gapless state at $W_{c1}<W<W_{c2}$ with the band ordering $E2$-$H1$-$H2$-$E1$ at the Γ point conditionally corresponds to the BG state in the clean limit[28]. Thus, starting from a band insulator in the clean limit, the 2D system, under influence of disorder, successively passes into the BG state, and then into the HOTI state. This mimics a horizontal movement from left to right at the phase diagram in Fig. 1.

Let us now discuss the second band-gap closing, which occurs at $W > W_{c2}$. Figure 3(d) shows an energy dependence of the spectral function at the Γ point at different disorder strength. If the disorder strength only slightly exceeds the critical value W_{c2}, the spectral function shows pronounced peaks associated with quasiparticles from different subbands. Here, we underline the strongly asymmetrical non-Lorentzian shape of the peaks in $A(k = 0, \varepsilon)$. This signals that no perfectly coherent quasiparticles can be defined, and incoherent processes associated with the imaginary parts of the self-energy are relevant in the presence of disorder.

As W increases, the peaks corresponding to the $E1$ and $E2$ subbands at $W > W_{c2}$ broaden and merge into one, which shifts towards lower energies, while the peak defining the quasiparticles in the $H1$ subband shifts towards higher energies. Finally, with a further growth of W, the broadening of both peaks, corresponding to the electron-like and hole-like states, increases by so much that it leads to the band-gap closing at $W > 350$ meV·nm. At the same time, the peaks defining the electron- and hole-like subbands are still well separated even in the absence of a pronounced band gap. This behavior of the spectral function directly indicates that the band-gap closing is associated with the overlap of the DOS from different subbands.

Let us now briefly consider disorder-induced phase transitions in double HgTe QWs with single- and double-

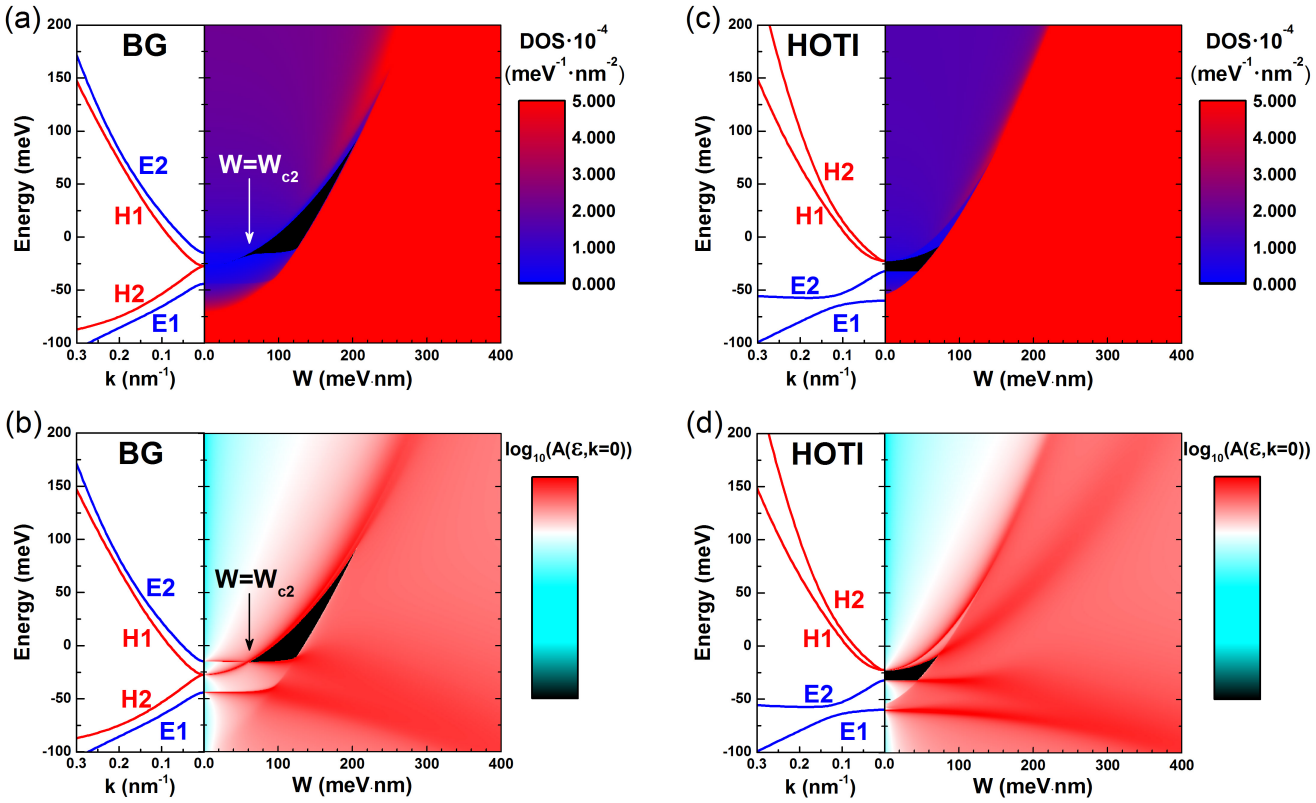

FIG. 4. (a,b) Band structure, DOS and spectral function at the Γ point $A(k=0,\varepsilon)$ as a function of the disorder strength $W=\sqrt{n_i}u_0$ for double HgTe QW hosting BG state at $W=0$ ($M_1<0$ and $M_2>0$, the structure "C" in Fig. 1). (c,d) The same as in (a) and (b) panels but for double HgTe QW hosting HOTI state in the absence of disorder ($M_1<0$ and $M_2<0$, the structure "E" in Fig. 1).

band-inversion in the absence of disorder (see the diagram in Fig. 1). Figure 4 provides the evolution of DOS and spectral function at the Γ point with the disorder strength for the structures "C" and "E", hosting BG and HOTI states in the clean limit, respectively. As seen from Fig. 4(a), the double HgTe QW with BG state maintains zero band-gap even in the presence of weak disorder. When the disorder strength reaches its critical value W_{c2}, a band-gap opens in the DOS. As clear from Fig. 4(b), this moment corresponds to the band inversion between $E2$ and $H2$ subbands. Such behavior of the spectral function unambiguously indicates that the 2D system at $W<W_{c2}$ is in the same topological state as at $W=0$, which is uniquely identified as the BG state. This indeed confirms the assumption made for the structure "A" that the gapless state in the range of $W_{c1}<W<W_{c2}$ is attributed to the BG state.

When W exceeds its critical value W_{c2}, the structure "C" becomes a double-inverted insulator, whose band-gap vanishes as the disorder strength increases further (cf. Fig. 3). A similar behavior of the band-gap is also seen in the DOS evolution for the structure "E" with a double-band inversion at $W=0$ as shown in Fig. 4(c). Thus, an increase in the disorder strength always leads to the band-gap vanishing of double-inverted insulator due to smearing of the edges of the conduction and valence subbands at high values of W. As clearly seen from Fig. 4(d), such band-gap behavior is caused primarily by smearing of the edges of the $E1$ and $H1$ bands at the Γ that leads to the DOS overlapping between conduction and valence subbands.

Finally, let us discuss the application of the obtained results to real samples[32–42] with double HgTe QWs. As clear from Fig. 2, the effective 2D low-energy model used for the calculation of DOS and spectral function can actually be applied to the states with the small values of $\mathbf{k}$. In this sense, the low-energy model used for double HgTe QWs is analogous to the BHZ model[1] proposed earlier for the low-energy states of single HgTe QWs in the vicinity of the Γ point of the Brillouin zone. At the same time, the calculation of the self-energy matrix within SCBA for the case of short-range scatterers requires the summation of all states in the entire Brillouin zone. The latter also involves a large range of quasimomentum values, far beyond the applicability of the effective 2D low-energy model. We emphasize that such an internal contradiction is also inherent in all previous studies performed on the basis of the BHZ model (including its tight-binding version)[14–17]. This perhaps explains why disorder-induced phase transitions theoretically studied in the previous

works have never been observed in solid state systems. Additionally, it is physically difficult to fine-tune the disorder in real semiconductor devices.

Fortunately, there are several non-solid-state systems implemented in cold atoms, photonic crystals and electrical circuits, whose entire Brillouin zone is fully described by a tight-binding version of the BHZ model. Recent experimental observation of TAI state in these systems[51–54] evidences that the results of current work can also be of interest for experimental verification in the "analogues" of double HgTe QWs also made on the basis of cold atoms[51], photonic crystals[52] and electric circuits[53,54].

V. SUMMARY

We have investigated the effect of disorder induced by short-range impurities on the band-gap of double HgTe QWs hosting trivial, single-band-inverted and double-band-inverted states in the clean limit. By using the SCBA and a four-band 2D low-energy Hamiltonian, we directly calculate the DOS and spectral function describing the quasiparticles at the Γ point of the Brillouin zone. By following the DOS and spectral function evolution when increasing the disorder strength, we unambiguously demonstrated multiple topological phase transitions caused by the mutual inversion of both first and second electron-like and hole-like subbands. We have found out that an increase in the disorder strength in the double-inverted state always leads to the band-gap closing due to the overlap of the tails of DOS from conduction and valence subbands. Experimental observations of the disorder-induced phase transitions in non-solid-state systems based on cold atoms, photonic crystals and electric circuits evidence that the results of current work can also be of interest for experimental verification in the "analogues" of double HgTe QWs made on the basis of the mentioned systems.

ACKNOWLEDGMENTS

This work was supported by the Terahertz Occitanie Platform, by the CNRS through IRP "TeraMIR" by the French Agence Nationale pour la Recherche ("Colector" project) and the Russian Science Foundation (Grant # 22-22-00382).

Appendix: Calculation of integrals in Eq. (19)

In order to calculate the integrals in Eq. (19), one should find four complex roots $x_1(\varepsilon)$, $x_2(\varepsilon)$, $x_3(\varepsilon)$ and $x_4(\varepsilon)$ of the polynomial in Eq. (20):

$$\left|\varepsilon - \tilde{H}_{4\times4}(\sqrt{x}) - \hat{\Sigma}(\varepsilon)\right| = A_4(\varepsilon)x^4 + A_3(\varepsilon)x^3 + A_2(\varepsilon)x^2 + A_1(\varepsilon)x + A_0(\varepsilon).$$

The latter is derived by straightforward calculation of 4×4 symmetric matrix determinant:

$$\begin{aligned}\det\left(\hat{A}\right) = {} & a_{12}^2a_{34}^2 - a_{33}a_{44}a_{12}^2 + 2a_{44}a_{12}a_{13}a_{23} - 2a_{12}a_{13}a_{24}a_{34} - 2a_{12}a_{14}a_{23}a_{34} + 2a_{33}a_{12}a_{14}a_{24} - a_{22}a_{33}a_{14}^2 \\ & + a_{13}^2a_{24}^2 - a_{22}a_{44}a_{13}^2 - 2a_{13}a_{14}a_{23}a_{24} + 2a_{22}a_{13}a_{14}a_{34} + a_{14}^2a_{23}^2 - a_{11}a_{44}a_{23}^2 + 2a_{11}a_{23}a_{24}a_{34} - a_{11}a_{33}a_{24}^2 \\ & - a_{11}a_{22}a_{34}^2 + a_{11}a_{22}a_{33}a_{44}. \qquad \text{(A.1)}\end{aligned}$$

Once the roots are known, the *complex* integrals in Eq. (19) are calculated as

$$\begin{aligned}\int \frac{ax^3+bx^2+cx+d}{A_4(x-x_1)(x-x_2)(x-x_3)(x-x_4)}dx = {} & \frac{ax_1^3+bx_1^2+cx_1+d}{A_4(x_1-x_2)(x_1-x_3)(x_1-x_4)}\ln(x-x_1) \\ & + \frac{ax_2^3+bx_2^2+cx_2+d}{A_4(x_2-x_1)(x_2-x_3)(x_2-x_4)}\ln(x-x_2) + \frac{ax_3^3+bx_3^2+cx_3+d}{A_4(x_3-x_1)(x_3-x_2)(x_3-x_4)}\ln(x-x_3) \\ & + \frac{ax_4^3+bx_4^2+cx_4+d}{A_4(x_4-x_1)(x_4-x_2)(x_4-x_3)}\ln(x-x_4). \qquad \text{(A.2)}\end{aligned}$$

* These authors contributed equally to this work

† frederic.teppe@umontpellier.fr

[1] B. A. Bernevig, T. L. Hughes, and S.-C. Zhang, Science **314**, 1757 (2006).
[2] L. G. Gerchikov and A. V. Subashiev, Phys. Status Solidi B **160**, 443 (1990).
[3] B. Büttner, C. Liu, G. Tkachov, E. Novik, C. Brüne, H. Buhmann, E. Hankiewicz, P. Recher, B. Trauzettel, S. Zhang, and L. Molenkamp, Nat. Phys. **7**, 418 (2011).
[4] M. Zholudev, F. Teppe, M. Orlita, C. Consejo, J. Torres, N. Dyakonova, M. Czapkiewicz, J. Wróbel, G. Grabecki, N. Mikhailov, S. Dvoretskii, A. Ikonnikov, K. Spirin, V. Aleshkin, V. Gavrilenko, and W. Knap, Phys. Rev. B **86**, 205420 (2012).
[5] S. Wiedmann, A. Jost, C. Thienel, C. Brüne, P. Leubner, H. Buhmann, L. W. Molenkamp, J. C. Maan, and U. Zeitler, Phys. Rev. B **91**, 205311 (2015).
[6] A. V. Ikonnikov, S. S. Krishtopenko, O. Drachenko, M. Goiran, M. S. Zholudev, V. V. Platonov, Y. B. Kudasov, A. S. Korshunov, D. A. Maslov, I. V. Makarov, O. M. Surdin, A. V. Philippov, M. Marcinkiewicz, S. Ruffenach, F. Teppe, W. Knap, N. N. Mikhailov, S. A. Dvoretsky, and V. I. Gavrilenko, Phys. Rev. B **94**, 155421 (2016).
[7] M. Marcinkiewicz, S. Ruffenach, S. S. Krishtopenko, A. M. Kadykov, C. Consejo, D. B. But, W. Desrat, W. Knap, J. Torres, A. V. Ikonnikov, K. E. Spirin, S. V. Morozov, V. I. Gavrilenko, N. N. Mikhailov, S. A. Dvoretskii, and F. Teppe, Phys. Rev. B **96**, 035405 (2017).
[8] A. M. Kadykov, S. S. Krishtopenko, B. Jouault, W. Desrat, W. Knap, S. Ruffenach, C. Consejo, J. Torres, S. V. Morozov, N. N. Mikhailov, S. A. Dvoretskii, and F. Teppe, Phys. Rev. Lett. **120**, 086401 (2018).
[9] S. S. Krishtopenko, I. Yahniuk, D. B. But, V. I. Gavrilenko, W. Knap, and F. Teppe, Phys. Rev. B **94**, 245402 (2016).
[10] C. L. Kane and E. J. Mele, Phys. Rev. Lett. **95**, 146802 (2005).
[11] M. König, S. Wiedmann, C. Brüne, A. Roth, H. Buhmann, L. W. Molenkamp, X.-L. Qi, and S.-C. Zhang, Science **318**, 766 (2007).
[12] I. Knez, R.-R. Du, and G. Sullivan, Phys. Rev. Lett. **107**, 136603 (2011).
[13] S. Wu, V. Fatemi, Q. D. Gibson, K. Watanabe, T. Taniguchi, R. J. Cava, and P. Jarillo-Herrero, Science **359**, 76 (2018).
[14] J. Li, R.-L. Chu, J. K. Jain, and S.-Q. Shen, Phys. Rev. Lett. **102**, 136806 (2009).
[15] C. W. Groth, M. Wimmer, A. R. Akhmerov, J. Tworzydło, and C. W. J. Beenakker, Phys. Rev. Lett. **103**, 196805 (2009).
[16] L. Chen, Q. Liu, X. Lin, X. Zhang, and X. Jiang, New J. of Phys. **14**, 043028 (2012).
[17] A. Girschik, F. Libisch, and S. Rotter, Phys. Rev. B **88**, 014201 (2013).
[18] S. S. Krishtopenko, M. Antezza, and F. Teppe, Phys. Rev. B **101**, 205424 (2020).
[19] H.-M. Guo, G. Rosenberg, G. Refael, and M. Franz, Phys. Rev. Lett. **105**, 216601 (2010).
[20] K. Kobayashi, T. Ohtsuki, and K.-I. Imura, Phys. Rev. Lett. **110**, 236803 (2013).
[21] S. Ryu and K. Nomura, Phys. Rev. B **85**, 155138 (2012).
[22] C.-Z. Chen, J. Song, H. Jiang, Q.-f. Sun, Z. Wang, and X. C. Xie, Phys. Rev. Lett. **115**, 246603 (2015).
[23] H. Shapourian and T. L. Hughes, Phys. Rev. B **93**, 075108 (2016).
[24] S. Bera, J. D. Sau, and B. Roy, Phys. Rev. B **93**, 201302 (2016).
[25] M. J. Park, B. Basa, and M. J. Gilbert, Phys. Rev. B **95**, 094201 (2017).
[26] S. S. Krishtopenko, M. Antezza, and F. Teppe, Phys. Rev. B **106**, 115203 (2022).
[27] C. Wang, T. Cheng, Z. Liu, F. Liu, and H. Huang, Phys. Rev. Lett. **128**, 056401 (2022).
[28] S. S. Krishtopenko, W. Knap, and F. Teppe, Sci. Rep. **6**, 30755 (2016).
[29] F. Schindler, A. M. Cook, M. G. Vergniory, Z. Wang, S. S. P. Parkin, B. A. Bernevig, and T. Neupert, Sci. Adv. **4**, eaat0346 (2018).
[30] F. Schindler, Z. Wang, M. G. Vergniory, A. M. Cook, A. Murani, S. Sengupta, A. Yu., Kasumov, R. Deblock, S. Jeon, I. Drozdov, H. Bouchiat, S. Guéron, A. Yazdani, B. A. Bernevig, and T. Neupert, Nat. Phys. **15**, 918 (2018).
[31] Z. Wang, B. J. Wieder, J. Li, B. Yan, and B. A. Bernevig, Phys. Rev. Lett. **123**, 186401 (2019).
[32] M. V. Yakunin, S. S. Krishtopenko, S. M. Podgornykh, M. R. Popov, V. N. Neverov, N. N. Mikhailov, and S. A. Dvoretsky, JETP Lett. **104**, 403 (2016).
[33] S. M. Podgornykh, M. V. Yakunin, S. S. Krishtopenko, M. R. Popov, N. N. Mikhailov, and S. A. Dvoretskii, Semiconductors **53**, 919 (2019).
[34] M. V. Yakunin, S. S. Krishtopenko, W. Desrat, S. M. Podgornykh, M. R. Popov, V. N. Neverov, S. A. Dvoretsky, N. N. Mikhailov, F. Teppe, and B. Jouault, Phys. Rev. B **102**, 165305 (2020).
[35] G. M. Gusev, E. B. Olshanetsky, F. G. G. Hernandez, O. E. Raichev, N. N. Mikhailov, and S. A. Dvoretsky, Phys. Rev. B **101**, 241302 (2020).
[36] G. M. Gusev, E. B. Olshanetsky, F. G. G. Hernandez, O. E. Raichev, N. N. Mikhailov, and S. A. Dvoretsky, Phys. Rev. B **103**, 035302 (2021).
[37] I. Nikolaev, A. Kazakov, K. Drozdov, M. Bannikov, K. Spirin, R. Menshchikov, S. Dvoretsky, N. Mikhailov, D. Khokhlov, and A. Ikonnikov, J. Appl. Phys. **132**, 234301 (2022).
[38] M. K. Sotnichuk, A. S. Kazakov, I. D. Nikolaev, K. A. Drozdov, R. V. Menshchikov, S. A. Dvoretsky, N. N. Mikhailov, D. R. Khokhlov, and A. V. Ikonnikov, Photonics **10**, 877 (2023).
[39] L. S. Bovkun, S. S. Krishtopenko, A. V. Ikonnikov, V. Y. Aleshkin, A. M. Kadykov, S. Ruffenach, C. Consejo, F. Teppe, W. Knap, M. Orlita, B. Piot, M. Potemski, N. N. Mikhailov, S. A. Dvoretskii, and V. I. Gavrilenko, Semiconductors **50**, 1532 (2016).
[40] L. S. Bovkun, A. V. Ikonnikov, V. Y. Aleshkin, S. S. Krishtopenko, N. N. Mikhailov, S. A. Dvoretskii, M. Potemski, B. Piot, M. Orlita, and V. I. Gavrilenko, JETP Lett. **108**, 329 (2018).
[41] L. S. Bovkun, A. V. Ikonnikov, V. Y. Aleshkin, K. V. Maremyanin, N. N. Mikhailov, S. A. Dvoretskii, S. S. Krishtopenko, F. Teppe, B. A. Piot, M. Potemski, M. Orlita, and V. I. Gavrilenko, Opto-electron. Rev. **27**, 213 (2019).
[42] A. V. Ikonnikov, S. S. Krishtopenko, L. S. Bovkun, N. N. Mikhailov, S. A. Dvoretskii, B. A. Piot, M. Potemski, M. Orlita, F. Teppe, and V. I. Gavrilenko, JETP Lett. **116**, 547 (2022).
[43] S. S. Krishtopenko, Sci. Rep. **11**, 21060 (2021).
[44] S. S. Krishtopenko and F. Teppe, Sci. Adv. **4**, eaap7529 (2018).
[45] E. L. Ivchenko, A. Y. Kaminski, and U. Rössler, Phys. Rev. B **54**, 5852 (1996).

[46] A. M. Kadykov, F. Teppe, C. Consejo, L. Viti, M. S. Vitiello, S. S. Krishtopenko, S. Ruffenach, S. V. Morozov, M. Marcinkiewicz, W. Desrat, N. Dyakonova, W. Knap, V. I. Gavrilenko, N. N. Mikhailov, and S. A. Dvoretsky, Appl. Phys. Lett. **107**, 152101 (2015).

[47] A. M. Kadykov, J. Torres, S. S. Krishtopenko, C. Consejo, S. Ruffenach, M. Marcinkiewicz, D. But, W. Knap, S. V. Morozov, V. I. Gavrilenko, N. N. Mikhailov, S. A. Dvoretsky, and F. Teppe, Appl. Phys. Lett. **108**, 262102 (2016).

[48] I. Yahniuk, S. S. Krishtopenko, G. Grabecki, B. Jouault, C. Consejo, W. Desrat, M. Majewicz, A. M. Kadykov, K. E. Spirin, V. I. Gavrilenko, N. N. Mikhailov, S. A. Dvoretsky, D. B. But, F. Teppe, J. Wrobel, G. Cywinski, S. Kret, T. Dietl, and W. Knap, npj Quantum Mater. **4**, 13 (2019).

[49] S. Mantion, C. Avogadri, S. S. Krishtopenko, S. Gebert, S. Ruffenach, C. Consejo, S. V. Morozov, N. N. Mikhailov, S. A. Dvoretskii, W. Knap, S. Nanot, F. Teppe, and B. Jouault, Phys. Rev. B **102**, 075302 (2020).

[50] S. S. Krishtopenko, A. M. Kadykov, S. Gebert, S. Ruffenach, C. Consejo, J. Torres, C. Avogadri, B. Jouault, W. Knap, N. N. Mikhailov, S. A. Dvoretskii, and F. Teppe, Phys. Rev. B **102**, 041404 (2020).

[51] E. J. Meier, F. A. An, A. Dauphin, M. Maffei, P. Massignan, T. L. Hughes, and B. Gadway, Science **362**, 929 (2018).

[52] S. Stützer, Y. Plotnik, Y. Lumer, P. Titum, N. H. Lindner, M. Segev, M. C. Rechtsman, and A. Szameit, Nature **560**, 461 (2018).

[53] Z.-Q. Zhang, B.-L. Wu, J. Song, and H. Jiang, Phys. Rev. B **100**, 184202 (2019).

[54] W. Zhang, D. Zou, Q. Pei, W. He, J. Bao, H. Sun, and X. Zhang, Phys. Rev. Lett. **126**, 146802 (2021).